Monthly Notices
of the
ROYAL ASTRONOMICAL SOCIETY

MNRAS **462,** 2847–2860 (2016)
Advance Access publication 2016 July 25

doi:10.1093/mnras/stw1802

The supermassive black hole and double nucleus of the core elliptical NGC 5419

Ximena Mazzalay,[1⋆] Jens Thomas,[1,2] Roberto P. Saglia,[1,2] Gary A. Wegner,[3] Ralf Bender,[1,2] Peter Erwin,[1] Maximilian H. Fabricius[1,2,4] and Stephanie P. Rusli[1,2]

[1]*Max-Planck-Institut für extraterrestrische Physik, Postfach 1312, D-85741 Garching, Germany*
[2]*Universitätssternwarte, Scheinerstrasse 1, D-81679 München, Germany*
[3]*Department of Physics and Astronomy, Dartmouth College, 6127 Wilder Laboratory, Hanover, NH 03755, USA*
[4]*Subaru Telescope, 650 North Aohoku Place, Hilo, HI 96720, USA*

Accepted 2016 July 21. Received 2016 July 8; in original form 2015 October 17

ABSTRACT

We obtained adaptive-optics assisted SINFONI observations of the central regions of the giant elliptical galaxy NGC 5419 with a spatial resolution of 0.2 arcsec (≈55 pc). NGC 5419 has a large depleted stellar core with a radius of 1.58 arcsec (430 pc). *HST* and SINFONI images show a point source located at the galaxy's photocentre, which is likely associated with the low-luminosity AGN previously detected in NGC 5419. Both the *HST* and SINFONI images also show a second nucleus, off-centred by 0.25 arcsec (≈70 pc). Outside of the central double nucleus, we measure an almost constant velocity dispersion of $\sigma \sim 350\,\mathrm{km\ s^{-1}}$. In the region where the double nucleus is located, the dispersion rises steeply to a peak value of $\sim$420 km s^{-1}. In addition to the SINFONI data, we also obtained stellar kinematics at larger radii from the South African Large Telescope. While NGC 5419 shows low rotation ($v < 50\,\mathrm{km\ s^{-1}}$), the central regions (inside $\sim 4\,r_\mathrm{b}$) clearly rotate in the opposite direction to the galaxy's outer parts. We use orbit-based dynamical models to measure the black hole mass of NGC 5419 from the kinematical data outside of the double nuclear structure. The models imply $M_\mathrm{BH} = 7.2^{+2.7}_{-1.9} \times 10^9\ \mathrm{M}_\odot$. The enhanced velocity dispersion in the region of the double nucleus suggests that NGC 5419 possibly hosts two supermassive black holes at its centre, separated by only ≈70 pc. Yet our measured M_BH is consistent with the black hole mass expected from the size of the galaxy's depleted stellar core. This suggests, that systematic uncertainties in M_BH related to the secondary nucleus are small.

Key words: galaxies: individual: NGC 5419 – galaxies: kinematics and dynamics – galaxies: nuclei.

1 INTRODUCTION

It is now well established that super massive black holes (SMBHs) are present at the centres of galaxies with bulges. The observational correlations found between the black hole mass and various parameters of the host galaxy, e.g. velocity dispersion, bulge mass, and bulge luminosity, have led to the idea that the formation and evolution of early-type galaxies and their nuclear SMBHs are tightly linked (see e.g. Kormendy & Ho 2013, and references therein).

NGC 5419 is a luminous elliptical galaxy ($M_V = -23.1$). Such bright early-type galaxies (brighter than $M_V \sim -21$) often have a low-density 'core' with a typical size of a few tens or hundreds of parsecs. Inside the core or break radius, r_b, the light profile is much shallower than the inward extrapolation of the outer Sérsic profile (e.g. Lauer et al. 1995, 2005; Graham et al. 2003; Rusli et al. 2013b). Moreover, core galaxies differ from fainter ellipticals in their isophotal shapes and degree of rotational support: core ellipticals have boxy instead of discy isophotes and are supported by anisotropic velocity dispersions rather than rotational stellar motions (e.g. Nieto, Bender & Surma 1991; Kormendy & Bender 1996; Faber et al. 1997; Lauer 2012). These morphological and kinematic distinctions between core galaxies and fainter ellipticals suggest that the processes involved in their formation are different.

The most plausible mechanism for core formation is black hole scouring that occurs in non-dissipative mergers of galaxies as a result of the dynamics of their central SMBHs: the SMBHs spiral into the centre of the merger via dynamical friction, ultimately forming a black hole binary (Begelman, Blandford & Rees 1980). As the binary shrinks, it ejects stars on intersecting orbits, creating a low-density core with a mass deficit of the order of or a few times larger than the mass of the binary (see e.g. Milosavljević

⋆ E-mail: ximena@mpe.mpg.de

& Merritt 2001; Merritt 2006, 2013, and references therein). The black hole binary model can explain the correlations between core structure, black hole masses, mass deficits, and the observed orbital structure in core galaxies (e.g. Faber et al. 1997; Milosavljević & Merritt 2001; Hopkins et al. 2009; Kormendy & Bender 2009; Thomas et al. 2014, 2016). Dissipation-driven core formation has been reported from numerical *N*-body simulations that include the dynamical effects of AGN feedback, but these results have not been tested yet in detail against the wealth of observations available for core elliptical galaxies.

Core scouring implies the formation of black hole binaries. Their subsequent evolution can follow different paths. In particular, if the binary separation decreases enough and the SMBHs manage to coalesce, the merged black hole could be ejected from the galaxy centre by anisotropic emission of gravitational waves (e.g. Begelman et al. 1980). As the probability that the remnant black hole recoils at a velocity exceeding the escape velocity of a large elliptical galaxy is low (e.g. Lousto et al. 2012), it will most likely remain bound to the galaxy on a radial orbit. On the other hand, if the binary decay stalls, subsequent mergers may bring a third SMBH or second black hole binary to the centre (e.g. Valtonen 1996). The interactions of this newly formed multiple SMBH system will eventually displace one or more of the SMBHs from the nucleus. In both of these scenarios, off-centred SMBHs are expected to be found in the centre of bright elliptical galaxies. The observational evidence of binary or recoiled SMBHs that supports these theoretical predictions is still scarce, usually involving pairs of SMBHs at kiloparsec separations (e.g. Komossa et al. 2003; Ballo et al. 2004; Bianchi et al. 2008; Fu et al. 2011; Koss et al. 2011; Comerford et al. 2015; McGurk et al. 2015). On smaller scales, mostly indirect evidence has been reported, with only one secure case known so far (CSO 0402+379, Rodriguez et al. 2006).

In this paper we study NGC 5419, the dominant galaxy of the poor cluster Abell 753. This large elliptical galaxy was first classified as a core by Lauer et al. (2005), who modelled its inner ∼10 arcsec surface brightness profile derived from an *HST*/WFPC2 *F555W* image. Based on a Nuker-law (Lauer et al. 1995) fit to NGC 5419 profile, they derived a break radius $r_b = 2.38$ arcsec (650 pc), making this relatively low surface brightness core the largest among the 42 objects classified as core galaxies in their sample. Moreover, the *HST* image presented by Lauer et al. (2005) revealed the presence of a double nucleus at the centre of the galaxy, with a projected separation of a few tens of parsecs (see also Capetti, Verdoes Kleijn & Chiaberge 2005; Lena et al. 2014; this work). Additionally, radio observations (Goss et al. 1987; Subrahmanyan et al. 2003) and the detection of hard X-rays (Balmaverde, Capetti & Grandi 2006) indicate that the centre of NGC 5419 hosts a low-luminosity AGN (LLAGN). All this makes NGC 5419 an interesting case for studying the interplay between core galaxies and their SMBHs.

We observed NGC 5419 as part of our black hole survey, consisting of 30 galaxies observed with SINFONI at the Very Large Telescope (VLT; Nowak et al. 2007, 2008, 2010; Rusli et al. 2011, 2013a,b; Saglia et al. 2016; Bender et al. in preparation; Erwin et al. in preparation; Thomas et al. in preparation). Here we report the results obtained for NGC 5419. The SINFONI data of NGC 5419 and additional long-slit spectroscopy from the Southern African Large Telescope (SALT) are presented in Section 2. In Sections 3 and 4, we present the results from the imaging and spectroscopy of NGC 5419. Section 5 deals with the dynamical modelling of the galaxy. A discussion about the double nucleus of NGC 5419 can be found in Section 6 and our final conclusions in Section 7.

We assume a distance to NGC 5419 of 56.2 Mpc, derived from the radial velocity corrected for Local Group infall on to Virgo taken from Hyperleda, $v_{vir} = 4047\,km\,s^{-1}$, and a value of $H_0 = 72\,km\,s^{-1}\,Mpc^{-1}$. At this distance, 1 arcsec corresponds to 273 pc.

2 OBSERVATIONS AND DATA REDUCTION

2.1 SINFONI IFS data

Adaptive-optics-assisted near-infrared (NIR) observations of NGC 5419 were obtained with the SINFONI integral field spectrograph at the 8 m VLT UT4 on 2009 May 20–24. A field of view (FOV) of ∼3 × 3 arcsec (820 × 820 pc) was covered at a spatial sampling of 0.05 × 0.10 arcsec^2 pixel^{-1} in the *K* band (1.95–2.45 μm) with a spectral resolution of $R \sim 5000$. The observations were performed according to a standard object-sky-object strategy, followed by the observation of a point spread function (PSF) star to assess the adaptive optics (AO) performance and characterize the PSF (see e.g. Mazzalay et al. 2013; Rusli et al. 2013a). Individual 10 min exposures dithered by a few spatial pixels resulted in a total on-source exposure time of 250 min. During the observations, the AO was operated in the laser guide star mode. This improves the spatial resolution to ≈0.2 arcsec (55 pc), as given by the full width at half-maximum (FWHM) of the PSF stars associated with the observations.

The SINFONI data were reduced using ESOREX (Modigliani et al. 2007), including all the standard reduction steps, i.e. bias subtraction, flat-fielding, bad pixel removal, detector distortion and wavelength calibration, sky subtraction (Davies 2007), reconstruction of the object data cubes and telluric correction. The data cubes were re-sampled to a spatial scale of 0.05 × 0.05 arcsec^2 pixel^{-1}. 25 data cubes were combined to produce one single final cube. The lower panel of Fig. 1 shows an example spectrum in the region of the Na I and CO absorption lines, obtained from the combination of the entire SINFONI FOV. No emission lines are observed in our data.

2.2 Long-slit SALT data

In addition to the NIR data for the centre, optical spectra along the position angles[1] PA = 78° (hereafter MJ axis) and PA = 168° (hereafter MN axis) were obtained at the 10 m SALT. The observations utilized the Robert Stobie Spectrograph in long slit mode (slit width 1.25 arcsec) and grating PG2300 covering the wavelength range 4800–5700 Å. The plate scale is 0.14 arcsec pix^{-1} and the spectral resolution, measured from the arc lamps, is FWHM ∼ 40 km s^{-1}. Three 850 s exposures were obtained on 2013 Mar 22 for MJ axis and two 1100 s exposures for MN axis were made on 2013 Apr 30. The bias-subtracted and flattened images provided by the SALT pipeline were wavelength calibrated in two dimensions by fitting ThAr and CuAr comparison spectra with fifth-order polynomials employing the long-slit menu in IRAF. Flux calibrations used the G93−48 standard in IRAF.

The upper panel of Fig. 1 shows an example SALT spectrum in the observed frame, obtained by summing up the signal over three pixels (0.42 arcsec) around the continuum maximum, and continuum normalized.

[1] Position angles are measured from north to east.

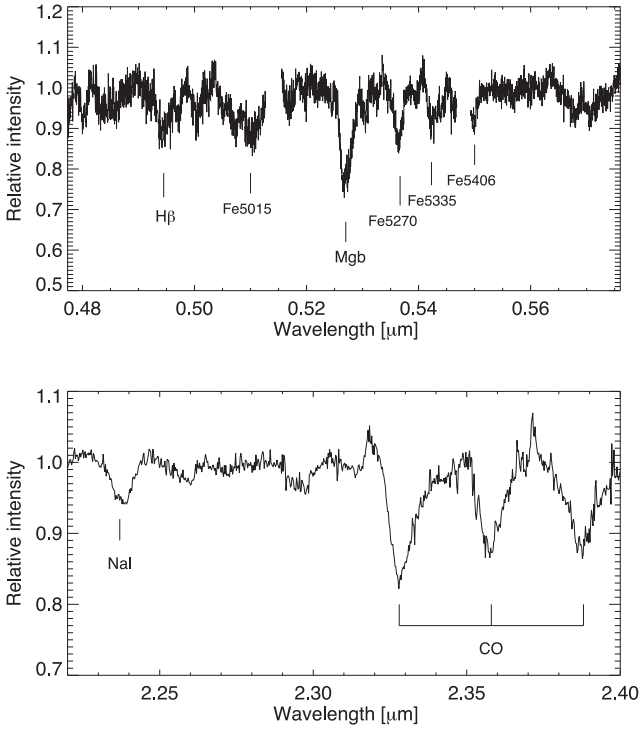

Figure 1. Optical (SALT, upper panel) and NIR (SINFONI, lower panel) continuum-normalized spectrum of NGC 5419, in the observed frame. The labels indicate the principal lines observed in the galaxy spectra.

3 THE LIGHT PROFILE: A DEPLETED CORE WITH A DOUBLE NUCLEUS

To study the light distribution of NGC 5419 we use *HST*/WFPC2 *F555W*[2] and 3.6 μm *Spitzer* IRAC1[3] images retrieved from the archives, as well as our SINFONI collapsed cube. Overall, NGC 5419 shows a smooth light distribution, with no signs of obvious distortions that could indicate a recent merger or the presence of dust. The *HST* image shows what appears to be a double nucleus at the centre of the galaxy (upper-left panel of Fig. 2), first seen by Lauer et al. (2005) and Capetti et al. (2005). The brighter of the two nuclei, N1, is located at the galaxy's photocentre.[4] It is unresolved in the *HST* image and is likely associated with the LLAGN of NGC 5419. The second nucleus, N2, is seen in the form of a bright blob, off-centred by approximately 0.25 arcsec (70 pc) towards the south, almost aligned with the semiminor axis of the galaxy. The off-centre nucleus has a Gaussian FWHM of ≈0.15 arcsec, slightly larger than the *HST* PSF (0.07 arcsec). Additionally, a 'bridge' of weak emission is observed between the two nuclei, suggesting that they are physically related and that their proximity is not merely a projection effect.

3.1 The depleted stellar core in NGC 5419

The surface brightness profile of NGC 5419 was constructed by fitting ellipses to the *HST* and *Spitzer* images. For this we employed the task ellipse of the STSDAS package of IRAF. As a first step, we used a rescaled *HST* PSF to subtract the central point source N1 from the *HST* image. The scaling factor was computed iteratively to make the slope of the light profile inside 0.2 arcsec consistent with the one around 1 arcsec. Once N1 was subtracted (upper-right panel of Fig. 2), we derived the final *HST* profile masking N2, as well as several globular clusters. Finally, the *HST* and *Spitzer* profiles were matched by determining the scaling and sky value that minimize the magnitude square differences between the two profiles in the 5–18 arcsec range. Since the galaxy fills the entire *HST* FOV, the sky background was estimated from the larger *Spitzer* image. Fig. 3 shows the final surface brightness profile, with and without point source, calibrated to Cousins *R* band using the aperture photometry reported by Poulain & Nieto (1994). The scaled *HST* PSF is also included.

The remaining light profile of NGC 5419 without the two compact central sources is well described by a Core-Sérsic function (e.g. Graham et al. 2003; Trujillo et al. 2004; Rusli et al. 2013b). This is shown in Fig. 3, where we plot the surface brightness profile together with the corresponding Core-Sérsic fit and its residuals. The best-fitting model has a Sérsic index $n = 7.2$, a projected half-light radius $r_e = 110.8$ arcsec, a core break radius $r_b = 1.58$ arcsec, a surface brightness at the break radius of $\mu_b = 17.09$ mag arcsec^2, a flat inner slope $\gamma = 0.09$ and a transition parameter $\alpha = 3.22$. Note that the Core-Sérsic fit provides a much better description of NGC 5419's light profile than a simple Sérsic model, and clearly identifies this galaxy as a core elliptical (e.g. Rusli et al. 2013b). Given these parameters, we can estimate the light deficit in the core from the luminosity difference between the best-fitting Core-Sérsic model and its Sérsic component. We follow Rusli et al. (2013b) and obtain a *R*-band luminosity deficit of $(3.78 \pm 0.15) \times 10^9$ L$_\odot$ (assuming an extinction correction of $A_R = 0.193$). This corresponds to $M_R = -19.5$ mag or $M_V = -18.8$ mag (with $V - R = 0.67$ from Poulain & Nieto 1994).

3.2 The double nucleus as seen by SINFONI

The double nucleus mentioned above has only been detected in the optical with *HST* thus far. Although they are not resolved, these two nuclei are also seen in our SINFONI data. The lower-left panel of Fig. 2 shows a zoom into the central $r \sim 0.5$ arcsec (135 pc) of the SINFONI image of NGC 5419 centred at the continuum maximum. The *K*-band isophotes are overlaid. Taking into account the differences in spatial resolution between the *HST* and SINFONI images, it is clear that the elongation of the isophotes near the centre is the result of the presence of the secondary nucleus.

We used these images to derive the $V - K$ colour of the different components in the centre of NGC 5419. We calibrated the *HST* image to the *V* band in the Johnson system using the transformation from Holtzman et al. (1995) and calibrated the SINFONI collapsed cube to the *K* band using a 2MASS image. We degraded the spatial resolution and pixel scale of the *HST* image to match those of our SINFONI data and created a $V - K$ colour map. The upper panel of Fig. 4 shows a close-up around N1 and N2 of the resulting $V - K$ colour map. The contours correspond to the *HST* isophotes. The central point source stands out from the rest of the galaxy by its bluer colour. While the galaxy colour, measured in regions further away from N1 and N2, varies from ≈2.99to3.02, N1 has a colour $V - K \approx 2.8$. However, this value does not represent that of N1 alone, since it also includes light from the galaxy. Similarly as for the *HST* image, we subtracted the central point source from the SINFONI image (lower-right panel of Fig. 2) and derived the intrinsic $V - K$ colour of N1 from the integrated magnitudes of the

[2] proposal ID = 6587, PI = D. Richstone
[3] program ID = 30318, PI = G. Fazio
[4] A low-significance displacement of 0.6 pixel (0.02 arcsec) between the central point-source and the galaxy's photocentre of NGC 5419 is reported by Lena et al. (2014).

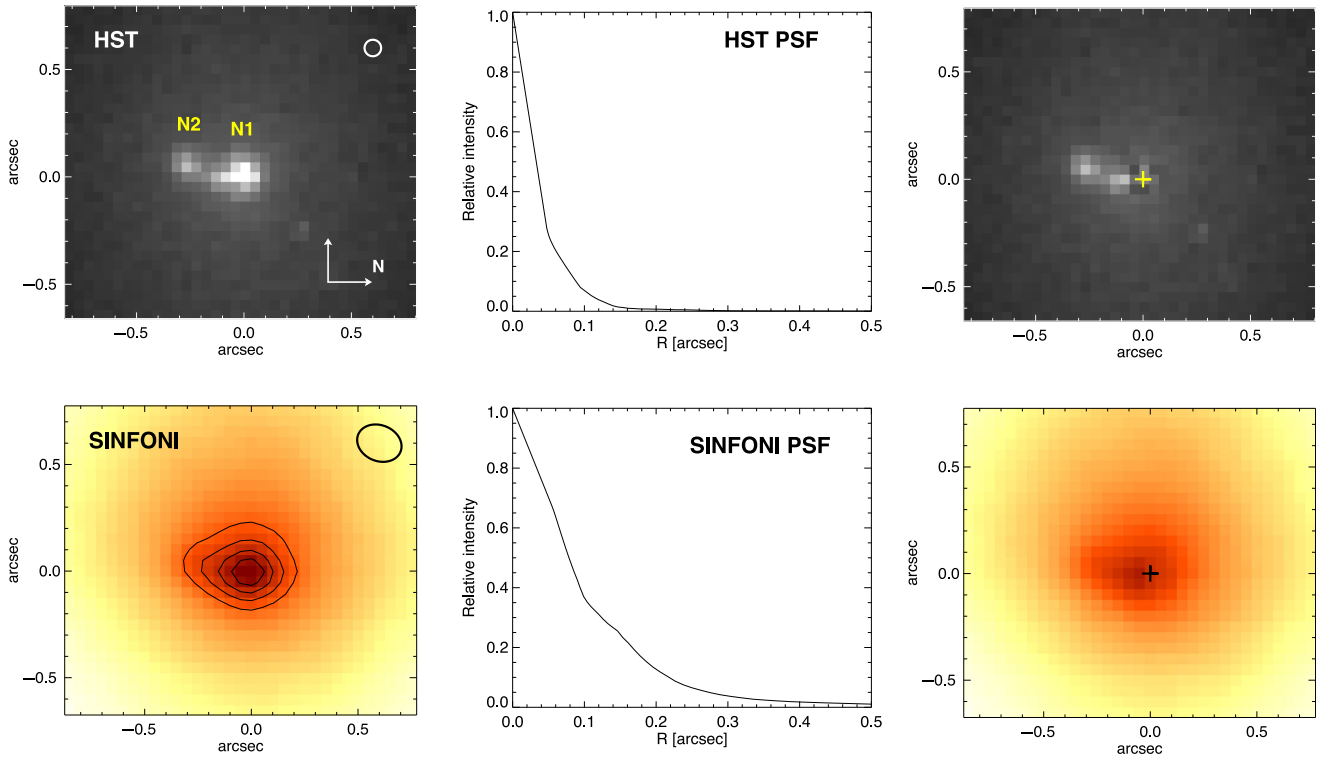

Figure 2. Close-up of the inner 1.5 × 1.5 arcsec (410 × 410 pc) of NGC 5419. Left-hand panels: *HST*/WFPC2 *F555W* image and *K* band VLT/SINFONI collapsed cube and isophotes. The images are centred at the position of the continuum maximum; the spatial orientation is indicated in the upper panel. N1 and N2 denote the central point source and the off-centre nucleus, respectively. The ellipses on the upper-right corners of the images indicate the Gaussian FWHM of the respective PSFs. Central and right panels show the corresponding PSF profiles and point-source-subtracted images.

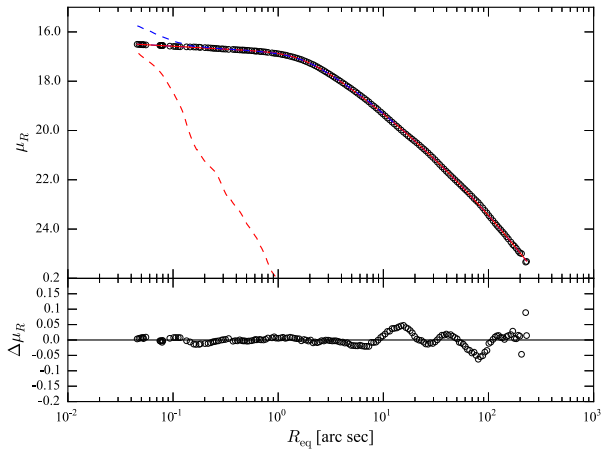

Figure 3. Surface brightness profile (circles), best-fitting Core-Sérsic model (red solid line) and residuals. The blue and red dashed curves correspond to the *HST* surface brightness profile of NGC 5419 before the point source subtraction and the rescaled *HST* PSF profile, respectively (see Section 3.1 for details).

HST and SINFONI rescaled PSFs. Unlike in the optical, N1 is not prominent in the *K* band (it accounts for only ∼5 per cent of the light coming from the inner $r = 0.15$ arcsec), resulting in a relative blue colour of $V - K = 1.13$.

The lower-panel of Fig. 4 shows again the $V - K$ colour map but this time with the central point source subtracted. A decrease of the $V - K$ colour can be clearly seen around the region where the secondary nucleus is located. To obtain its intrinsic colour we isolated the light from N2 by subtracting from the N1-subtracted *HST* and SINFONI images a galaxy model constructed from the ellipse-fitting results and measured the magnitudes in an aperture of $r = 0.15$ arcsec (40 pc) centred at N2. The absolute magnitudes of N2 in the *V* and *K* bands are $M_V = -11.93$ and $M_K = -13.61$, corresponding to luminosities of $L_V = 4.9 \times 10^6$ $L_\odot$ and $L_K = 5.7 \times 10^6$ $L_\odot$. The intrinsic colour of N2 is thus $V - K = 1.68$. While the colour of NGC 5419 is typical of an old early type galaxy (e.g. Bower, Lucey & Ellis 1992), the off-centre nucleus would correspond to a younger stellar population.

A summary of the measured luminosities and colours of the central point source and the off-centre nucleus are given in Table 1. All values have been corrected for Galactic extinction ($A_V = 0.199$ and $A_K = 0.022$ from NED).

3.3 Stellar mass of the off-centre nucleus

Assuming that the luminosity of N2 is entirely of stellar origin, we use the single stellar population (SSP) models of Maraston (1998, 2005) to derive some of its basic properties. For a Salpeter initial mass function (IMF), the colour of N2 corresponds to a metal-poor, ∼2 Gyr old stellar population with a *V*-band mass-to-light ratio $M/L_V \simeq 1$. This M/L_V ratio together with the derived luminosity implies a stellar mass for the off-centre nucleus of about 5×10^6 $M_\odot$ inside a region of ≈40 pc of radius.

Our stellar mass estimate lies in the range of extremely massive clusters and low-mass dwarf galaxies and ultracompact dwarfs (e.g. Walcher et al. 2005; Erwin et al. 2015). Given the blue colour and young age, it is unlikely that N2 is a massive globular cluster. Globular clusters in early-type galaxies are typically old (ages $\gtrsim$ 10 Gyr; e.g. Hempel et al. 2007; Chies-Santos et al. 2011), although

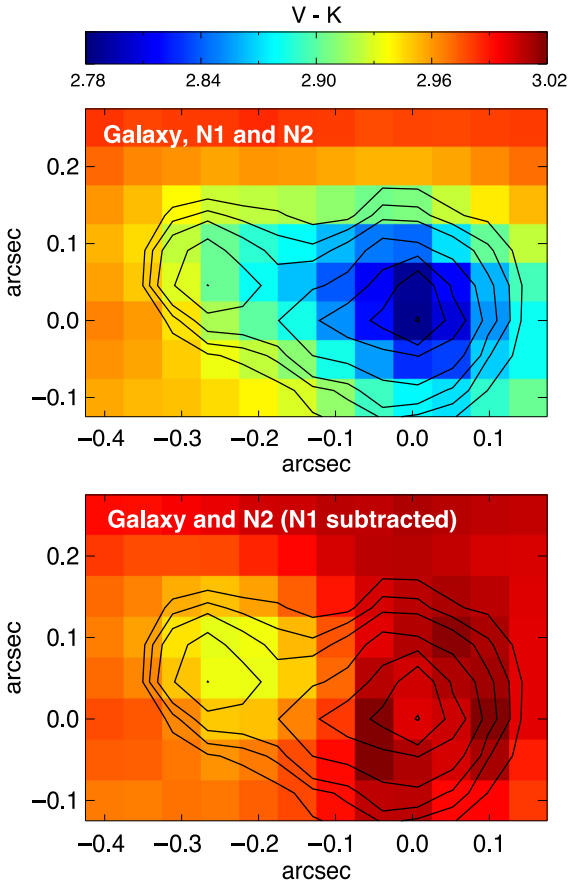

Figure 4. $V-K$ colour maps derived from the *HST* and SINFONI images before (upper panel) and after (lower panel) the subtraction of the central point source. The contours correspond to the *HST* isophotes (see Fig. 2). North is right, east is up.

Table 1. Luminosities and colour of the central point source N1 and the off-centre nucleus N2 measured inside apertures of 0.15 arcsec in radius. The $V-K$ colour of the galaxy is also included for comparison.

	L_V ($L_\odot$)	L_K ($L_\odot$)	$V-K$
N1	1.3×10^7	9.2×10^6	1.13
N2	4.9×10^6	5.7×10^6	1.68
Galaxy	–	–	∼3

younger clusters (∼2–8 Gyr) have been claimed in a few cases (e.g. Goudfrooij et al. 2001; Puzia et al. 2002; Hempel et al. 2003). Even an intermediate-age cluster is unlikely, since they usually have a $V-K>2$. We can further compare the V-band magnitude of N2 with those of the other clusters observed in the *HST* image of NGC 5419. Their magnitude does not vary much from cluster to cluster, with a mean value of $M_V=-10.45\pm0.60$ mag estimated from 10 clusters. These are relatively bright compared to, for example, the ones found in the Milky Way or M31. Still, N2 is about an order of magnitude brighter. Therefore it is unlikely that the off-centre nucleus is a globular cluster.

It is possible that some fraction of the light we see is due to AGN emission, and that the colour of the stellar population in the secondary nucleus is in fact redder than assumed here. This would imply a higher mass-to-light ratio. However, even in the most extreme cases, the stellar mass would only increase by a factor of 5.

4 KINEMATICS AND LINE STRENGTH MEASUREMENTS

In order to obtain the kinematic information of NGC 5419 we used two different data sets: SINFONI integral field spectroscopic (IFS) data covering the inner regions of the galaxy with high spatial resolution and long-slit SALT data obtained along the MJ and MN axis providing information out to ∼15 arcsec. In the following sections we describe the extraction of the kinematics from these data sets and the results. Particular care was taken in estimating the contribution from non-stellar emission to the NIR continuum, which could bias the derived kinematics. Additionally, in Section 4.4 we measure optical line indices to study the stellar populations.

4.1 SINFONI kinematics: a high dispersion region near the centre

Non-parametric line-of-sight velocity distributions (LOSVDs) were derived using a maximum penalized likelihood technique (MPL; Gebhardt et al. 2000). We apply the approach described in detail by Nowak et al. (2007, 2008). In brief, a set of late-type stellar template spectra (observed with SINFONI in the same configuration as the galaxy) were convolved with the LOSVDs in order to match the continuum-subtracted galaxy spectra in the region of the first two CO bandheads [^{12}CO(2−0) and ^{12}CO(3−1)]. Only stars with CO equivalent widths ($W_{\rm CO}$) similar to the galaxy were used in the fitting to minimize template mismatch. In order to have a relatively high signal-to-noise ratio (SNR; at least ∼40), the individual spectra of the galaxy were combined using a radial and angular binning scheme following Gebhardt et al. (2003). The uncertainties in the derived LOSVDs were estimated from a set of 100 Monte Carlo simulations of the galaxy spectra. These were created by adding different amounts of noise to the best fitting stellar template convolved with the derived LOSVD.

While the non-parametric LOSVDs are used in the dynamical modelling (see Section 5), it is illustrative to express the LOSVD in Gauss–Hermite moments. Fig. 5 shows the velocity, velocity dispersion, h_3 and h_4 maps derived from the parametrization of the LOSVDs by Gauss–Hermite expansions up to order 4. The terms h_3 and h_4 quantify the asymmetric and symmetric deviations of the LOSVDs from a Gaussian function, respectively. The SINFONI kinematic maps show that NGC 5419 is dispersion dominated, with a velocity dispersion around ∼350 km s^{-1} and rotational motions with an amplitude of no more than ∼50 km s^{-1}. h_4 is predominantly negative over the entire SINFONI FOV.

The velocity dispersion map of Fig. 5 shows a hint of an increase in σ in the innermost bins ($r\lesssim0.4$ arcsec), almost reaching 450 km s^{-1}. To explore this in more detail, we relaxed the constraint on the minimum required SNR defining our binning scheme and derived the kinematics for the inner $r\sim0.5$ arcsec again. In order to preserve as much of spatial information as possible and, at the same time, ensure a SNR high enough to obtain meaningful kinematic parameters, we integrated the spectra over a circular aperture of $r=2$ pixels at each spatial position. Fig. 6 shows the velocity and velocity dispersion maps of the inner $r\sim0.5$ arcsec obtained in this way. Since the SNR of the spectrum at each pixel is relatively low, the resulting maps are rather noisy. However, there is an extended region with a high velocity dispersion at the centre. It is elongated in the N–S direction and seems associated with the two nuclei in the centre, approximately following the isophotes derived from the *HST* image (see Section 3). We note that the extent of this region is much larger than the SINFONI PSF shown by the white ellipse.

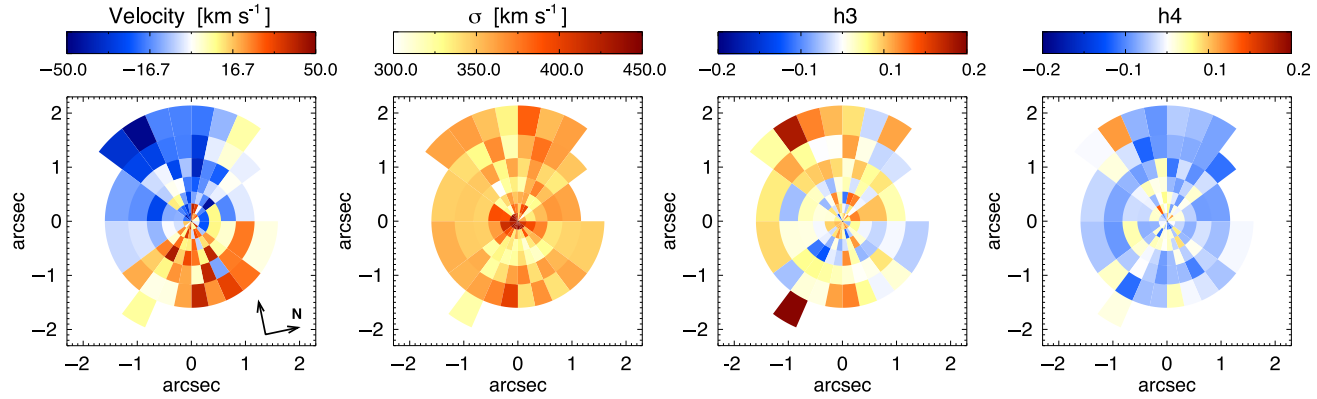

Figure 5. Kinematic maps of NGC 5419 derived from the SINFONI data. The spatial orientation is indicated in the left-hand panel; the major axis of the galaxy is aligned with the *y*-axis.

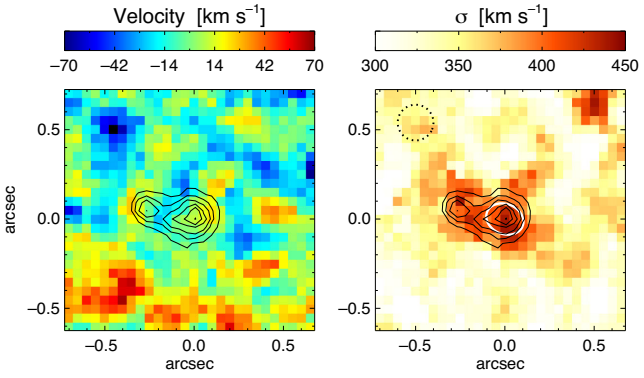

Figure 6. Velocity and velocity dispersion maps of the inner region of NGC 5419 derived from the SINFONI data. North is right and east is up. Overplotted are the isophotes of the *HST* image (see Fig. 2). The dashed circle and white ellipse in the right-hand panel indicate the binning size and the Gaussian FWHM of the SINFONI PSF, respectively.

Unlike in the dispersion map, there is no particular pattern in the rotational velocity in the innermost 100 pc of NGC 5419.

4.2 Is the non-stellar continuum affecting our kinematic measurements?

NGC 5419 is known to harbour a LLAGN at its centre. Many early-type galaxies contain compact, high-brightness temperature radio cores associated with LLAGNs and, in a few cases, parsec-scale jets are also observed (see e.g. Ho 2008, and references therein). While there is no evidence of a well-defined jet on scales of arcseconds or higher in NGC 5419, this galaxy does have a compact radio core ($r < 0.7$ arcsec; e.g. Goss et al. 1987; Subrahmanyan et al. 2003) similar to those typically found in LLAGNs. It is possible, then, that the off-centre nuclear structure is a jet similar to the optical jet observed in M87.

Since we are interested in the kinematics of the stars, which is sensitive to the equivalent width of the CO lines, it is important to determine how much this quantity is altered by the presence of a non-stellar continuum. For a stellar population that contains late-type stars, it has been shown that the W_{CO} is rather independent of the star formation history and age (e.g. Davies et al. 2007); any additional contribution to the NIR from a non-stellar continuum will dilute the W_{CO}. In order to estimate the contribution from non-stellar emission to the NIR continuum, we measured the equivalent width of the CO(2−0) line at 2.29 μm in the unbinned SINFONI spectra. Due to the low SNR of the individual spectra, the resulting W_{CO} map is rather noisy. However, it does not show any particular global pattern or any sign of a gradient towards either of the two nuclei, suggesting that the non-stellar emission coming from the centre is not enough to significantly alter the equivalent width of the CO. The W_{CO} is consistent with a constant value of 15.7 Å over the entire SINFONI FOV, with a standard deviation of 2.2 Å. We assume that this is the intrinsic W_{CO} of NGC 5419.

We can further compare this value with the ones measured from higher SNR spectra obtained by integrating our data in apertures of $r = 0.15$ arcsec centred at the position of the central point source N1 and the off-centre nucleus N2, $W_{CO} = 14.5 \pm 1.5$ and 15.3 ± 1.0, respectively. The maximum change in equivalent width is measured at N1, with a decrease of less than 10 per cent. This would be expected if the non-stellar continuum contributes about 10 per cent of the light in the CO region. Note that these numbers are consistent with the fractional light associated with N1, as estimated from the PSF subtraction of the SINFONI collapsed cube (see Section 3). Therefore, even if all the extra light at the galaxy's unresolved photocentre comes from an AGN, its contribution to the total light in the centre would be very small (at most 10 per cent) and the change in the CO equivalent width would be negligible. We checked that a 10 per cent AGN contribution to the CO region has no effects on the derived stellar kinematics.

In summary, the amount of any non-stellar light in the centre of NGC 5419 is not enough to affect our kinematic measurements. Moreover, since the extended high-σ region at $r < 0.35$ arcsec (≈100 pc) is not an artefact related to uncorrected continuum emission, it is unlikely that the off-centre source is an optical jet. Additional evidence against the jet scenario comes from the comparison of the colour of N2 with that of the well-studied optical jet in M87. The mean $V - K$ value of M87's jet is close to 1 (Zeilinger, Moller & Stiavelli 1993; Stiavelli, Peletier & Carollo 1997), much bluer than the value of 1.68 we obtained for N2 (Section 3.2).

4.3 Long-slit kinematics: a counter rotating core

To recover the full LOSVD from the SALT data we used the Fourier correlation method (FCQ; Bender 1990). While this method has the advantage of minimizing template mismatch, since it operates in Fourier space, the masking of spectral regions is problematic. Therefore, to avoid masking the spectral regions of the gap between the SALT detector chips, we derived the kinematics using only the

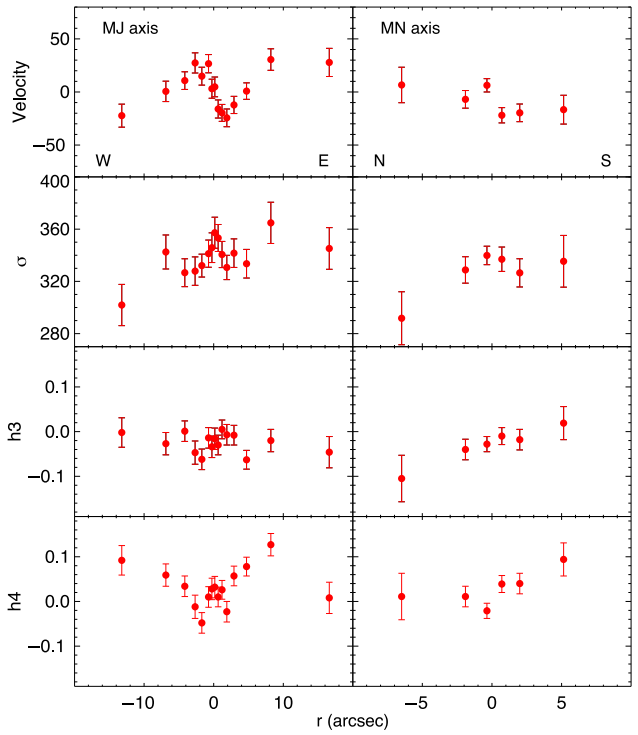

Figure 7. Stellar kinematics along the major (MJ) and minor (MN) axes derived from the SALT data. Positive radii indicate projected distances E and S from the centre for the MJ and MN axes, respectively.

5135–5431Å range, where the strongest absorption features are observed (e.g. Mgb, Fe5270). The SALT spectra were binned along the spatial direction to achieve a minimum SNR of 30 per Å at all radii. We used a 10 Gyr old synthetic stellar spectrum as kinematic template (Vazdekis et al. 2010). The uncertainties in the kinematic parameters were estimated from Monte Carlo simulations of synthetic spectra with artificial noise, based on the best-fitting set of parameters for each spectrum. Our stellar kinematic measurements along the MJ and MN axes, are shown in Fig. 7.

The kinematics derived from the SALT data in the inner $r \sim 2$ arcsec is consistent with what is seen with SINFONI: NGC 5419 shows little rotation and a velocity dispersion of $\sim$350 km s^{-1}. In fact, while the overall rotation amplitude is low, the long-slit data reveal that the outer parts of the galaxy ($r > 5$ arcsec) are rotating in the opposite direction as the centre. The transition region, where the sign of the angular momentum flips, is at $r \sim 5$–6 arcsec or roughly four times the core radius r_b (see Section 3.1).

4.4 Line indices and stellar population analysis

The wavelength range covered by SALT allows us to measure H β, Mgb5175, Fe5270, and Fe5335 line strength indices. These lines are known to be useful to constrain the age (particularly H β) and the chemical composition of the stellar population. Other lines in the SALT range that are commonly used to constrain stellar population parameters are Fe5015 and Fe5406. However, these lines are observed at the edges of the gaps between the detector chips (see Fig. 1) and were not included in the following analysis.

The Mg, Fe, and H β line strength indices were derived for the binned spectra along the MJ and MN axis using the same synthetic star spectrum as for the kinematics. Its resolution was degraded to match that of the Lick system, and the galaxy's velocity dispersions measured in the previous section were also taken into account. We used the band definitions of Worthey et al. (1994). In the following we indicate the average iron index with $\langle \mathrm{Fe} \rangle = (\mathrm{Fe5270} + \mathrm{Fe5335})/2$. To assess how well our measurements agree with the Lick system, we measured the line strength in several SSP model spectra from Vazdekis (1999) multiplied by the SALT instrumental response and compared them with their Lick indices values. The largest discrepancy was found for the Fe5335 index, in which case we found a difference of 0.76 Å between our measurement and the value given by Vazdekis (1999). The measured indices were corrected by these systemic offsets, and are shown in Fig. 8.

We study the stellar population using the SSP models of the Lick line indices of Maraston (1998, 2005) with a Kroupa IMF. These models cover ages of up 15 Gyr, metallicities [*Z*/H] from −2.25 to +0.67 and overabundances [α/Fe] from −0.3 to +0.5 (Thomas, Maraston & Bender 2003). We follow the procedure of Saglia et al. (2010, see their Section 4.1). At each radius, the age, metallicity, and overabundance were derived by fitting the SSP models to the three line indices. Fig. 8 shows the resulting age, metallicity, and overabundance derived from the line indices. We also include colours and M/L ratios for different bands corresponding to the best-fitting SSP models. The models fit well the measured indices except for the case of H β, which is too low to be reproduced by the models, especially at larger radii. As a result, the age of the stellar population is found to be the maximum age explored by the models, 15 Gyr (panel *e* of Fig. 8). This is usually regarded as an effect of ionized gas emission, which partly fills the hydrogen absorption lines, leading to a weaken measurement of the H β index and, therefore, an overestimation of the age of the stellar population. We do not see any evidence of gas emission in our spectra. However, Macchetto et al. (1996) reported the detection of weak H α +[N II] emission in the inner few arcsecond ($r \lesssim 5$ arcsec) of NGC 5419.

Overall, the models point to an old, metal-rich, slightly α/Fe-overabundant galaxy. The inferred $B - V$, $U - B$, and $V - R$ colours agree reasonable well with those reported from broad-band photometry ($B - V = 1.08$, $U - B = 0.68$, and $V - R = 0.67$ for $r = 11.4$ arcsec; Poulain & Nieto 1994), while the $V - K$ colour is similar to, though slightly redder than (possibly due to the overestimation of the stellar age) the value of $\sim$3 measured from the *HST* and SINFONI data (Section 3). The mass-to-light ratios are around 9, 5, and 4 $M_\odot/L_\odot$ for the *B*, *V*, and *R* bands, respectively (assuming a Kroupa IMF).

5 DYNAMICAL MODELLING

For the dynamical analysis of the SINFONI and SALT spectra we assumed that NGC 5419 is axisymmetric. The SINFONI data consists of 29 symmetric spatial bins in each quadrant. We first computed a folded kinematic data set by averaging the respective LOSVDs $\mathcal{L}$ of the four quadrants. The LOSVDs measured via MPL were sampled at 23 bins in the line-of-sight velocity $v_{\rm los}$. Each velocity channel was averaged individually, i.e. for a given $i \in [1, 23]$ we averaged the measured $\mathcal{L}_k(v_{\rm los,i})$ ($k = 1, \ldots, 4$) of the four quadrants, weighting each $\mathcal{L}_k$ by its error (and taking into account that v changes sign when crossing the galaxy's minor axis). We used these folded SINFONI kinematics together with the long-slit data from SALT as input for our dynamical models. The information contained in the wings of the LOSVDs is important for the estimation of the BH mass (e.g. Nowak et al. 2010, see also Appendix A).

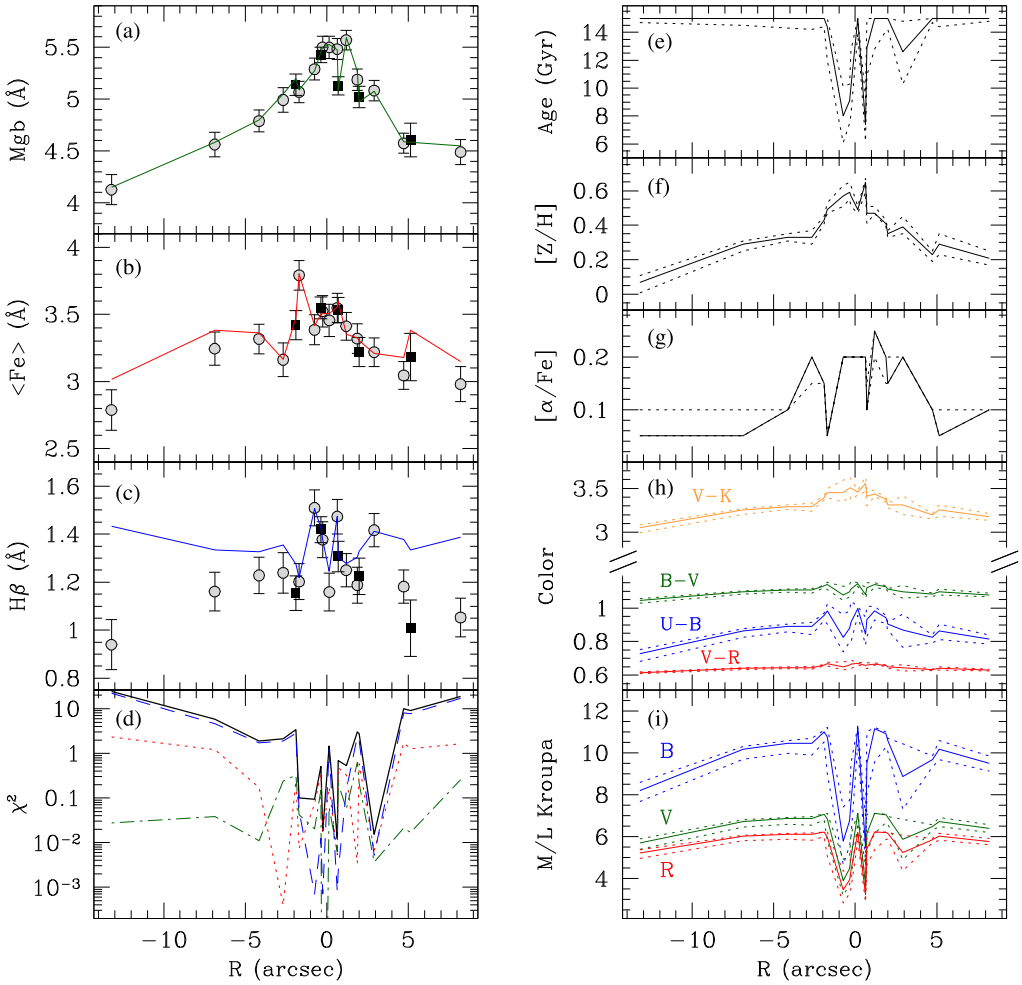

Figure 8. Panels (a)–(c): measured Lick indices profiles along the major (circles) and minor (squares) axes. The lines correspond to the best-fitting SSP models. Panel (d): χ^2 for each line index (the green dot–dashed line corresponds to Mgb, the red dotted line to Fe and the blue dashed line to H β) and the total χ^2 (black solid line). Panels (e)–(i): age, metallicity, overabundance, colours, and M/L in different bands as a function of radius. The dotted lines show the 3σ errors.

As discussed in Section 4.1, there is an extended region of high velocity dispersion in the innermost ≈100 pc of NGC 5419 (≈0.35 arcsec). It seems morphologically connected to the double nucleus in the centre. As the exact nature of this double nucleus is not clear at the moment (see Section 6), we decided to omit all kinematical data points inside $r < 0.35$ arcsec. Accordingly, we used the photometric galaxy model discussed in Section 3.1 as constraint for the light distribution in the orbit model. In this way, our model is independent of whether the enhanced velocity dispersion near the centre is a feature of the global stellar population of NGC 5419 or whether it comes from a separate stellar component with a different orbital structure (associated with the double nuclear structure).

We constructed equilibrium models for NGC 5419 using our implementation of Schwarzschild's orbit superposition method (Schwarzschild 1979; Richstone & Tremaine 1988; Gebhardt et al. 2003; Thomas et al. 2004, 2005). Schwarzschild models are very flexible and do not require any a priori assumptions upon the anisotropy of the stellar velocities. In brief, the model construction requires four steps.

(i) Deprojection of the observed surface brightness distribution to obtain the three-dimensional intrinsic stellar luminosity density j (Magorrian 1999).

(ii) Setup of a trial mass distribution:

$$\rho = \Upsilon \times j + \rho_{\rm DM} + \frac{M_{\rm BH}}{4\pi r^2} \times \delta(r), \quad (1)$$

assuming a stellar mass-to-light ratio Υ, a black hole mass $M_{\rm BH}$, and a parametrized dark matter (DM) halo density $\rho_{\rm DM}$ given by

$$\rho_{\rm DM} = \frac{v_{\rm c}^2}{4\pi G} \frac{3r_{\rm c}^2 + r^2}{(r_{\rm c}^2 + r^2)^2}, \quad (2)$$

where $r_{\rm c}$ is the core radius inside which the density slope of the DM is constant and $v_{\rm c}$ is the asymptotic circular velocity of the DM. $\delta(r)$ denotes Dirac's delta function.

(iii) Computation of a representative library of time-averaged stellar orbits.

(iv) Solving for the set of orbital weights or occupation numbers, respectively, that minimizes the χ^2 difference between the model and the observed LOSVDs.

These four steps are repeated, varying independently the free parameters of the model: Υ, $M_{\rm BH}$ and the parameters of the DM halo. The best-fitting $M_{\rm BH}$ and Υ and their errors are derived from a one-dimensional likelihood as in McConnell et al. (2011). We used ∼27 000 orbits to sample the space of integrals of motion for each trial ρ. For the dynamical fits, we used 125 constraints from the

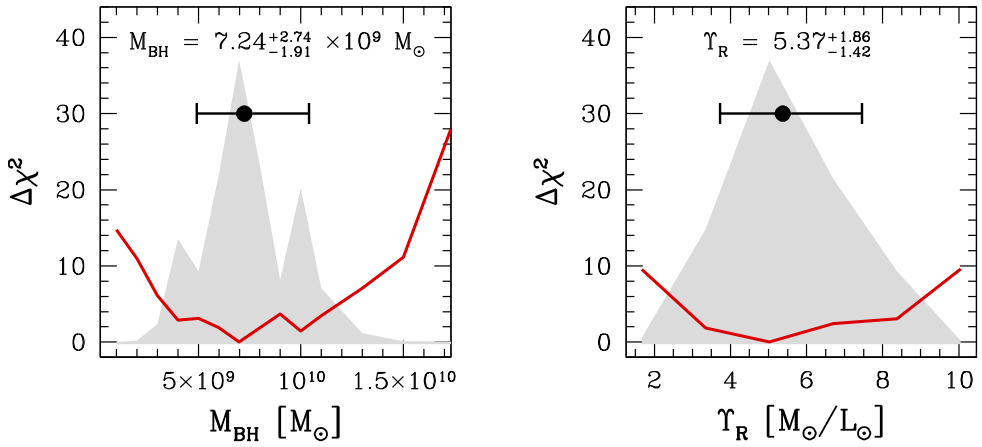

Figure 9. The χ^2 curves (solid red line) and model likelihoods (grey; arbitrarily scaled) versus black hole mass $M_{\rm BH}$ (left) and stellar mass-to-light ratio Υ (right; extinction corrected). The one-dimensional model statistics were computed following McConnell et al. (2011). The point with error bars indicates the best-fitting model and the 68 per cent confidence interval.

light distribution and 759 from the kinematic observations in the radial range $0.33 \leq r \leq 16.6$ arcsec. As noted above, we avoided the innermost LOSVDs because of the asymmetric structure visible in the SINFONI maps and in the *HST* image.

Our best-fitting model has $M_{\rm BH} = 7.24^{+2.74}_{-1.91} \times 10^9$ M$_\odot$ and an extinction-corrected R-band mass-to-light ratio of $\Upsilon = 5.37^{+1.86}_{-1.42}$ (see Fig. 9). Models without black hole and/or without DM halo are ruled out by a $\Delta\chi^2 > 20$ and 40, respectively. The evidence for the BH comes from the high velocity wings of the LOSVDs inside the BH's sphere of influence and the constraints on the orbit distribution at larger radii (Nowak et al. 2010; Rusli et al. 2013a, see also Appendix A). From the cumulative stellar mass distribution, we found a sphere-of-influence radius of NGC 5419's black hole – i.e. the radius at which the enclosed mass in stars equals the black hole mass – of $r_{\rm SOI} = 1.4$ arcsec. Thus, even when leaving out the very central data points, our measurements resolve the central black hole's sphere of influence by more than a factor of 4. We note that if the galaxy is triaxial then the BH mass of our axisymmetric model could be biased (van den Bosch & de Zeeuw 2010).

Fig. 10 shows the kinematics of the best-fitting model together with the (folded) data points. It also shows the innermost data points that we omitted in the fit and the inward extrapolation of the model into these regions. The model does not follow the strong increase in σ inside 0.35 arcsec. This is not surprising. The model is based on the fitted isophotes with the two nuclei in the centre masked or subtracted, respectively. The flat central core in the remaining light profile provides very little light in the centre that could cause a strong gradient. The flat σ distribution of the model near the centre, despite the presence of a massive black hole implied by the fit, together with the morphological connection of the high-σ region and the double nucleus suggests that the high dispersion near the centre comes from the extra light of one or both of the two nuclei. Without higher spatial resolution data, we cannot improve our model in the innermost regions.

5.1 SMBH and core properties

Since NGC 5419 is a core galaxy, we can investigate how well its SMBH correlates with the core properties. The strongest correlation found by Rusli et al. (2013b) was that between SMBH mass and core radius. The core radius of $r_{\rm b} = 1.58$ arcsec (≈430 pc) that we obtained from the fitting of a Core-Sérsic function to the surface brightness profile implies a black hole mass of $M_{\rm BH} \approx 6.4 \times 10^9$ M$_\odot$, in good agreement with our measurement. In other similar core galaxies a tight correlation between $r_{\rm SOI}$ and $r_{\rm b}$ has been found, with $r_{\rm SOI} = r_{\rm b}$ (Thomas et al. 2016). The $r_{\rm SOI} = 1.4$ arcsec and $r_{\rm b} = 1.58$ arcsec of NGC 5419 are consistent with this relation.

With the mass-to-light ratio given by the dynamical models and the light deficit estimated in Section 3 ($\Delta L_R = 3.78 \times 10^9$ L$_\odot$), we can also compute the stellar mass deficit in the core of NGC 5419. This is simply given by $M_{\rm def} = \Upsilon \times \Delta L = 2.0 \times 10^{10}$ M$_\odot$. The ratio between the mass deficit in the core and the black hole mass, $M_{\rm def}/M_{\rm BH} = 2.8$, is well within the range typically derived from observations and consistent with the theoretical predictions from simulations of single dry mergers (see Rusli et al. 2013b, and references therein).

6 THE DOUBLE NUCLEUS IN NGC 5419 AND HIGH DISPERSION REGIONS

In Section 3, we showed that the second nucleus observed previously in *HST* images is also seen in our SINFONI data. This structure, located at 0.25 arcsec (∼70 pc) from the unresolved central source, is relatively blue compared to the rest of the galaxy; we obtained $V - K = 1.68$ for the off-centre nucleus and ∼3 for the galaxy. Our SINFONI velocity dispersion map indicates a central region of high velocity dispersion ($\sigma \gtrsim 400$ km s^{-1}) that includes both nuclei and has a similar shape as the *HST* isophotes at $r \sim 0.35$ arcsec (Fig. 6). In Section 4.2, we ruled out the possibility that the steep central σ gradient connected with the two nuclei could be explained as an artefact related to non-stellar continuum emission associated with the LLAGN of NGC 5419. Thus, the high velocity dispersion near the centre likely has a dynamical origin. We modelled the galaxy assuming that the stars follow a Core-Sérsic surface brightness distribution, as indicated by the photometry at $r \gtrsim 0.4$ arcsec (Sections 3 and 5). The inward extrapolation of our best-fitting dynamical model does not, however, explain the excess central velocity dispersion as the result of the massive central black hole and the stellar orbits detected in the (cored) main body of NGC 5419. All this suggest that the high dispersion comes from a distinct stellar subsystem associated with the extra light in the double-nucleus region which we have omitted from the models.

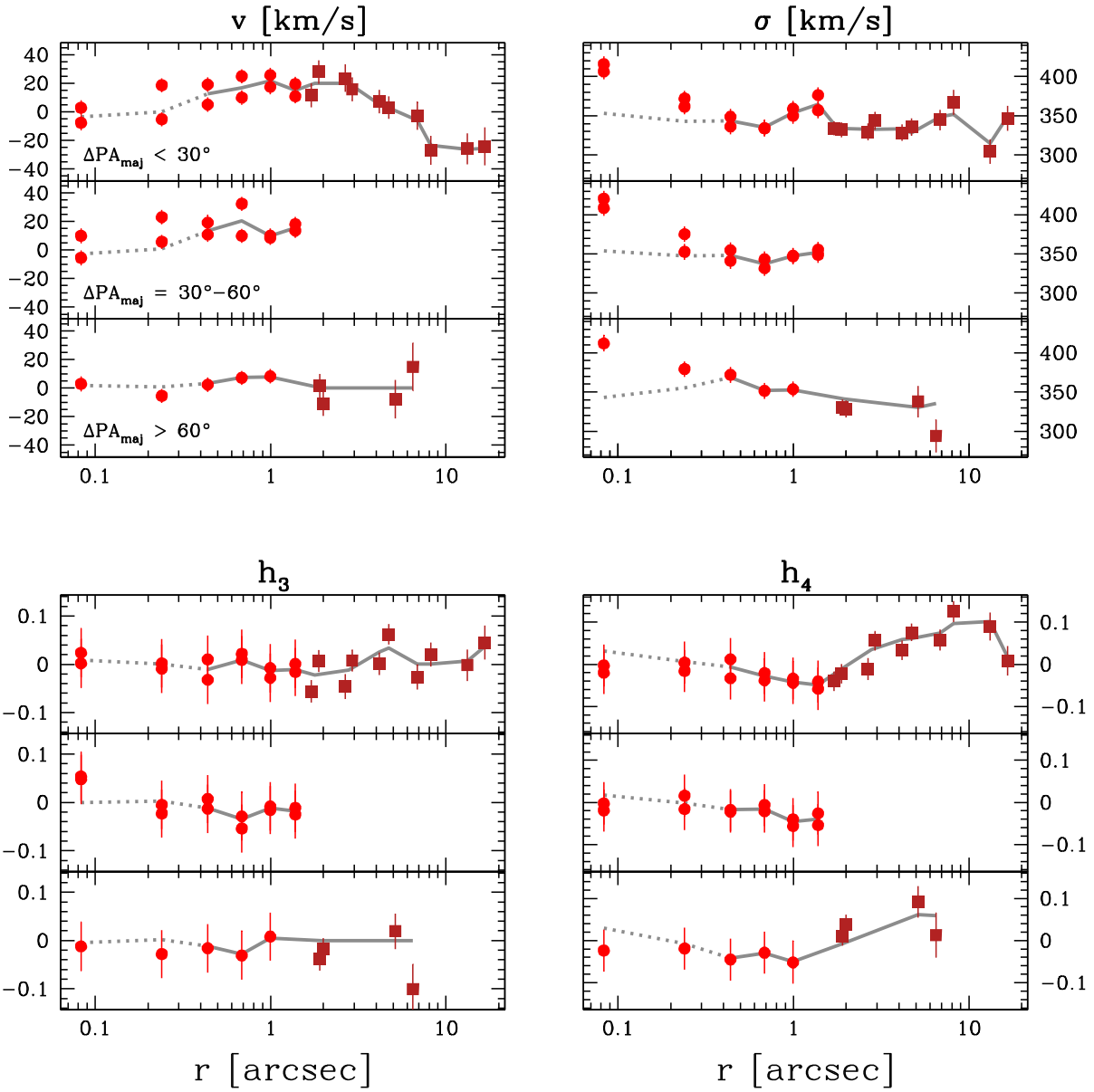

Figure 10. Kinematic data and the best-fitting model. Points with error bars show the SINFONI (red circles) and SALT (dark-red squares) folded kinematic data – from top-left to bottom-right: rotation velocity v, dispersion σ, and Gauss–Hermite parameters h_3 and h_4. Within each panel, data points are separated by the position angle (ΔPA_{maj}) relative to the galaxy's major axis. The grey solid lines indicate the best-fitting dynamical model. Data points inside $r < 0.35$ arcsec were omitted in the fit (see Section 5). The dotted lines show the inward extrapolation of the dynamical model down to the smallest measured radius. Note that for the dynamical modelling we use the full LOSVDs (Section 5), which is essential for constraining the BH mass (see discussion in Appendix A).

The colour difference between the two nuclear light peaks in NGC 5419 makes it unlikely that the eccentric, elongated high-velocity region is an asymmetric disc around a single black hole (similar to, though much larger, than the nuclear disk in M31; e.g. Tremaine 1995; Bender et al. 2005). Instead we assume that the high-σ stars originally formed a bound, undisturbed system around one of the nuclei and that the present elongated structure is the result of the two nuclei being in dynamical interaction. We can get an order-of-magnitude mass estimate for the original component from $\sigma^2 = GM_\star/r_\star$, where we assume that $r_\star$ is some 10 pc (upper limit from the larger of the two nuclear structures, N2; cf. Section 3). Together with the observed $\sigma = 400\,\mathrm{km\ s^{-1}}$ this points to a mass of about $M \sim 10^9\,M_\odot$, with an uncertainty probably as large as a factor of $\sim$10.

The light emitted by the off-centre nucleus N2 only accounts for a stellar mass of $\lesssim 10^7\,M_\odot$ (see Section 3.3). If the compact nuclear structure was originally associated with N2, then it immediately follows that N2 hosts a SMBH with a mass of the order of $10^9\,M_\odot$. Because of the lack of any gradient in the line-of-sight velocity of the high-σ stars, however, it seems more plausible that they were originally connected with the massive black hole at the galaxy's photocentre (i.e. at rest relative to the main body of NGC 5419). This would imply that a fraction of the spatially unresolved emission of N1 may still come from a very compact stellar

component, in addition to the galaxy's AGN. The fact that the interaction with N2 could (partly) dissolve this highly bound structure implies that N1 and N2 have roughly similar masses. In conclusion then, irrespective of whether the high-σ stars originally belonged to N1 or N2, the data presented here strongly suggest that there are two SMBHs of similar mass (to within a factor of $\sim$10) in the nucleus of NGC 5419, separated by a distance of only $\sim$70 pc.

If the centre of NGC 5419 really hosts two SMBHs, then N2 is probably the remain of a galaxy nucleus, which is also suggested by the fact that its colour and brightness are atypical for a globular cluster (Section 3.3). The light profile of NGC 5419 does not show obvious distortions that would indicate an ongoing merger, yet the kinematically decoupled core of NGC 5419 provides evidence for a (probably minor) merger in the galaxy's latest evolutionary phase. Since these mergers can last several Gyr (e.g. Boylan-Kolchin, Ma & Quataert 2008), we may be witnessing the last phase of such a minor merger. Note, however, that the lack of a systemic radial velocity difference between N1 and N2 implies a rather straight relative motion parallel to the plane of the sky, while on larger scales the observed counter rotation requires that at least some of the merger's orbital velocity was perpendicular to the plane of the sky.

If NGC 5419 is not in a late merger phase, could the two black holes have formed a stable, bound binary long ago? This is unlikely, since (for two circularly orbiting similar SMBHs) one would expect both black holes to be displaced from the centre of mass, i.e. the photocentre of the galaxy. Furthermore, the rather straight tidal feature seen between N1 and N2 and the lack of a gradient in the line-of-sight velocity would imply that the binary orbit has to be of low angular momentum and we must be seeing this binary very close to face-on, which is statistically unlikely.

A more exotic explanation for two black holes not being in a close orbit would be that we see a SMBH which was ejected from the centre on a low angular momentum orbit in a past multiple merger event and is now coming back from large radii. While this scenario is intrinsically unlikely too, the fast fly-by of N2 would account for a number of observational aspects of NGC 5419. First, it would explain why we only see a straight tidal feature between N2 and the central SMBH. Secondly, it would explain the fact that we cannot detect signs of an ongoing merger any more.

In summary, the increased velocity dispersion at $r \lesssim 0.35$ arcsec strongly suggests that NGC 5419 hosts two SMBHs in close proximity near the centre. However, we cannot reach a definitive picture for the origin of the perturber N2. The stellar kinematics at $r \gtrsim 0.35$ arcsec are consistent with a black hole mass of $M_{\rm BH} = 7.24^{+2.74}_{-1.91} \times 10^9$ $M_\odot$ located at the galaxy's photocentre (Section 5). That this $M_{\rm BH}$ is only slightly above the black hole mass we had expected if the galaxy were similar to other massive core ellipticals without a secondary nucleus suggests that the systematic uncertainties on $M_{\rm BH}$ related to N2 are small. Detailed numerical simulations and observations at a higher spatial resolution are required to put stronger constraints on the innermost mass distribution and on the origin of the two nuclei.

7 SUMMARY AND CONCLUSIONS

We have presented high-resolution *K*-band SINFONI/VLT IFS and optical long-slit spectroscopic observations of the galaxy NGC 5419. The kinematics derived from these data show that NGC 5419 is a dispersion-dominated galaxy. The rotational velocity does not exceed 50 km s^{-1}; although a clear rotational pattern is observed, revealing a counter-rotating core in the inner few arcseconds. The velocity dispersion is about 350 km s^{-1} and almost constant over the low-surface brightness core. However, inside 0.35 arcsec ($\approx$100 pc), where the galaxy hosts a double nucleus, it increases reaching values of 420–430 km s^{-1}.

We use orbit-based dynamical models to model the stellar kinematics outside the double nucleus in the centre. From this analysis we derive a $M_{\rm BH}$ of $7.24^{+2.74}_{-1.91} \times 10^9$ $M_\odot$. This mass is consistent with the large core radius ($r_{\rm b} = 1.58$ arcsec or $\approx$430 pc) obtained by fitting a Core-Sérsic function to the surface brightness profile, given the known correlation between core radius and SMBH mass (Rusli et al. 2013b).

The *R*-band mass-to-light ratio derived from the dynamical modelling, $\Upsilon = 5.37$, is about a factor of 1.1–1.4 larger than the one derived from the stellar population analysis in the inner few arcseconds, for which we assumed a Kroupa IMF. The dynamical Υ thus lies between a Kroupa and Salpeter IMF.

We have also discussed different scenarios in which the observed properties of the double nucleus of NGC 5419 can be explained. While the nature of the double nucleus in NGC 5419 is certainly puzzling, our observations suggest that this galaxy might host two SMBHs in close proximity. If this is the case, NGC 5419 is a promising target to study the interaction between SMBHs at the centre of galaxies, and their formation and evolution. More clues could be obtained from milliarcsecond radio imaging and higher spatial-resolution spectroscopic data, that would allow us to study in a resolved manner the structures seen in the central 0.5 arcsec (135 pc) of NGC 5419.

ACKNOWLEDGEMENTS

Some observations used in this paper were obtained from SALT under proposals 2012-1-DC-003 and 2012-2-DC-001. This paper is based on observations at the European Southern Observatory (ESO) Very Large Telescope [083.B-0126(B)]. This research has made use of the NASA/IPAC Extragalactic Database (NED) which is operated by the Jet Propulsion Laboratory of Technology, under contract with the National Aeronautics and Space. We acknowledge the usage of the Hyperleda database (http://leda.univ-lyon1.fr).

REFERENCES

Baes M., Dejonghe H., Buyle P., 2005, A&A, 432, 411
Ballo L., Braito V., Della Ceca R., Maraschi L., Tavecchio F., Dadina M., 2004, ApJ, 600, 634
Balmaverde B., Capetti A., Grandi P., 2006, A&A, 451, 35
Barth A. J., Boizelle B. D., Darling J., Baker A. J., Buote D. A., Ho L. C., Walsh J. L., 2016, ApJ, 822, L28
Begelman M. C., Blandford R. D., Rees M. J., 1980, Nature, 287, 307
Bender R., 1990, A&A, 229, 441
Bender R. et al., 2005, ApJ, 631, 280
Bianchi S., Chiaberge M., Piconcelli E., Guainazzi M., Matt G., 2008, MNRAS, 386, 105
Binney J., Mamon G. A., 1982, MNRAS, 200, 361 (BM82)
Binney J., Tremaine S., 2008, Galactic Dynamics, 2nd edn. Princeton Univ. Press, Princeton, NJ
Bower R. G., Lucey J. R., Ellis R. S., 1992, MNRAS, 254, 601
Boylan-Kolchin M., Ma C.-P., Quataert E., 2008, MNRAS, 383, 93
Capetti A., Verdoes Kleijn G., Chiaberge M., 2005, A&A, 439, 935
Cappellari M. et al., 2013, MNRAS, 432, 1709
Chies-Santos A. L., Larsen S. S., Kuntschner H., Anders P., Wehner E. M., Strader J., Brodie J. P., Santos J. F. C., 2011, A&A, 525, A20
Comerford J. M., Pooley D., Barrows R. S., Greene J. E., Zakamska N. L., Madejski G. M., Cooper M. C., 2015, ApJ, 806, 219

Davies R. I., 2007, MNRAS, 375, 1099
Davies R. I., Müller Sánchez F., Genzel R., Tacconi L. J., Hicks E. K. S., Friedrich S., Sternberg A., 2007, ApJ, 671, 1388
Erwin P. et al., 2015, MNRAS, 446, 4039
Faber S. M. et al., 1997, AJ, 114, 1771
Feldmeier A. et al., 2013, A&A, 554, A63
Fu H. et al., 2011, ApJ, 740, L44
Gebhardt K. et al., 2000, AJ, 119, 1157
Gebhardt K. et al., 2003, ApJ, 583, 92
Gerhard O. E., 1993, MNRAS, 265, 213
Goss W. M., McAdam W. B., Wellington K. J., Ekers R. D., 1987, MNRAS, 226, 979
Goudfrooij P., Alonso M. V., Maraston C., Minniti D., 2001, MNRAS, 328, 237
Graham A. W., Erwin P., Trujillo I., Asensio Ramos A., 2003, AJ, 125, 2951
Hempel M., Hilker M., Kissler-Patig M., Puzia T. H., Minniti D., Goudfrooij P., 2003, A&A, 405, 487
Hempel M., Kissler-Patig M., Puzia T. H., Hilker M., 2007, A&A, 463, 493
Ho L. C., 2008, ARA&A, 46, 475
Holtzman J. A., Burrows C. J., Casertano S., Hester J. J., Trauger J. T., Watson A. M., Worthey G., 1995, PASP, 107, 1065
Hopkins P. F., Lauer T. R., Cox T. J., Hernquist L., Kormendy J., 2009, ApJS, 181, 486
Komossa S., Burwitz V., Hasinger G., Predehl P., Kaastra J. S., Ikebe Y., 2003, ApJ, 582, L15
Kormendy J., Bender R., 1996, ApJ, 464, L119
Kormendy J., Bender R., 2009, ApJ, 691, L142
Kormendy J., Ho L. C., 2013, ARA&A, 51, 511
Koss M. et al., 2011, ApJ, 735, L42
Lauer T. R., 2012, ApJ, 759, 64
Lauer T. R. et al., 1995, AJ, 110, 2622
Lauer T. R. et al., 2005, AJ, 129, 2138
Lena D., Robinson A., Marconi A., Axon D. J., Capetti A., Merritt D., Batcheldor D., 2014, ApJ, 795, 146
Lousto C. O., Zlochower Y., Dotti M., Volonteri M., 2012, Phys. Rev. D, 85, 084015
Lyubenova M. et al., 2016, MNRAS, preprint (arXiv:1606.07448)
Macchetto F., Pastoriza M., Caon N., Sparks W. B., Giavalisco M., Bender R., Capaccioli M., 1996, A&AS, 120, 463
McConnell N. J., Ma C.-P., Graham J. R., Gebhardt K., Lauer T. R., Wright S. A., Richstone D. O., 2011, ApJ, 728, 100
McGurk R. C., Max C. E., Medling A. M., Shields G. A., Comerford J. M., 2015, ApJ, 811, 14
Magorrian J., 1999, MNRAS, 302, 530
Maraston C., 1998, MNRAS, 300, 872
Maraston C., 2005, MNRAS, 362, 799
Mazzalay X. et al., 2013, MNRAS, 428, 2389
Merritt D., 2006, ApJ, 648, 976
Merritt D., 2013, Dynamics and Evolution of Galactic Nuclei. Princeton Univ. Press, Princeton, NJ
Milosavljević M., Merritt D., 2001, ApJ, 563, 34
Modigliani A. et al., 2007, preprint (astro-ph/0701297)
Newman A. B., Treu T., Ellis R. S., Sand D. J., Nipoti C., Richard J., Jullo E., 2013, ApJ, 765, 24
Nieto J.-L., Bender R., Surma P., 1991, A&A, 244, L37
Nowak N., Saglia R. P., Thomas J., Bender R., Pannella M., Gebhardt K., Davies R. I., 2007, MNRAS, 379, 909
Nowak N., Saglia R. P., Thomas J., Bender R., Davies R. I., Gebhardt K., 2008, MNRAS, 391, 1629
Nowak N., Thomas J., Erwin P., Saglia R. P., Bender R., Davies R. I., 2010, MNRAS, 403, 646
Poulain P., Nieto J.-L., 1994, A&AS, 103, 573
Puzia T. H., Zepf S. E., Kissler-Patig M., Hilker M., Minniti D., Goudfrooij P., 2002, A&A, 391, 453
Richardson T., Fairbairn M., 2013, MNRAS, 432, 3361
Richstone D. O., Tremaine S., 1988, ApJ, 327, 82
Rodriguez C., Taylor G. B., Zavala R. T., Peck A. B., Pollack L. K., Romani R. W., 2006, ApJ, 646, 49
Rusli S. P., Thomas J., Erwin P., Saglia R. P., Nowak N., Bender R., 2011, MNRAS, 410, 1223
Rusli S. P. et al., 2013a, AJ, 146, 45
Rusli S. P., Erwin P., Saglia R. P., Thomas J., Fabricius M., Bender R., Nowak N., 2013b, AJ, 146, 160
Ryś A., van de Ven G., Falcón-Barroso J., 2014, MNRAS, 439, 284
Saglia R. P. et al., 2010, A&A, 509, A61
Saglia R. P. et al., 2016, ApJ, 818, 47
Schwarzschild M., 1979, ApJ, 232, 236
Scott N. et al., 2015, MNRAS, 451, 2723
Stiavelli M., Peletier R. F., Carollo C. M., 1997, MNRAS, 285, 181
Subrahmanyan R., Beasley A. J., Goss W. M., Golap K., Hunstead R. W., 2003, AJ, 125, 1095
Thomas D., Maraston C., Bender R., 2003, MNRAS, 339, 897
Thomas J., Saglia R. P., Bender R., Thomas D., Gebhardt K., Magorrian J., Richstone D., 2004, MNRAS, 353, 391
Thomas J., Saglia R. P., Bender R., Thomas D., Gebhardt K., Magorrian J., Corsini E. M., Wegner G., 2005, MNRAS, 360, 1355
Thomas J., Saglia R. P., Bender R., Erwin P., Fabricius M., 2014, ApJ, 782, 39
Thomas J., Ma C.-P., McConnell N. J., Greene J. E., Blakeslee J. P., Janish R., 2016, Nature, 532, 340
Tortora C., Napolitano N. R., Romanowsky A. J., Capaccioli M., Covone G., 2009, MNRAS, 396, 1132
Tremaine S., 1995, AJ, 110, 628
Trujillo I., Erwin P., Asensio Ramos A., Graham A. W., 2004, AJ, 127, 1917
Valtonen M. J., 1996, MNRAS, 278, 186
van den Bosch R. C. E., de Zeeuw P. T., 2010, MNRAS, 401, 1770
Vazdekis A., 1999, ApJ, 513, 224
Vazdekis A., Sánchez-Blázquez P., Falcón-Barroso J., Cenarro A. J., Beasley M. A., Cardiel N., Gorgas J., Peletier R. F., 2010, MNRAS, 404, 1639
Walcher C. J. et al., 2005, ApJ, 618, 237
Worthey G., Faber S. M., Gonzalez J. J., Burstein D., 1994, ApJS, 94, 687
Zeilinger W. W., Moller P., Stiavelli M., 1993, MNRAS, 261, 175

APPENDIX A: WHAT IS STELLAR DYNAMICAL EVIDENCE FOR A BH?

This appendix is the result of a request of the referee to present 'prima facie' evidence for the existence of a BH in NGC 5419, by showing the measured stellar kinematic second-order moments and the best-fitting models with and without a BH.

It has been known for 34 years (Binney & Mamon 1982, hereafter BM82) that centrally (i.e. near the BH sphere of influence) increasing stellar velocity dispersion profiles do not provide 'prima facie' evidence for BHs. This is different from the case of gaseous discs rotating around a BH, where a Keplerian increase of circular velocities near the sphere of influence is expected to mark the presence of the central BH (e.g. Barth et al. 2016). The recent increased popularity of the Jeans approach to study dynamical masses in stellar systems (e.g. Tortora et al. 2009; Cappellari et al. 2013; Newman et al. 2013; Feldmeier et al. 2013; Ryś, van de Ven & Falcón-Barroso 2014; Scott et al. 2015; Lyubenova et al. 2016) stresses the importance of modelling stellar second-order kinematic moments, but cannot exploit the information in the full stellar LOSVDs, which is the key to breaking the degeneracy between the gravitational potential and anisotropy pointed out by BM82, as discussed by Gerhard (1993).

BM82 showed that a centrally increasing stellar velocity dispersion profile, such as that produced by a stellar system with a BH and isotropic velocity dispersions for the stars, can also be produced by a system *without* a BH, if the velocity dispersions have radial anisotropy that is centrally increasing. Here we reconsider this case and add two further examples: a centrally decreasing velocity dispersion profile and a system with a flat velocity dispersion.

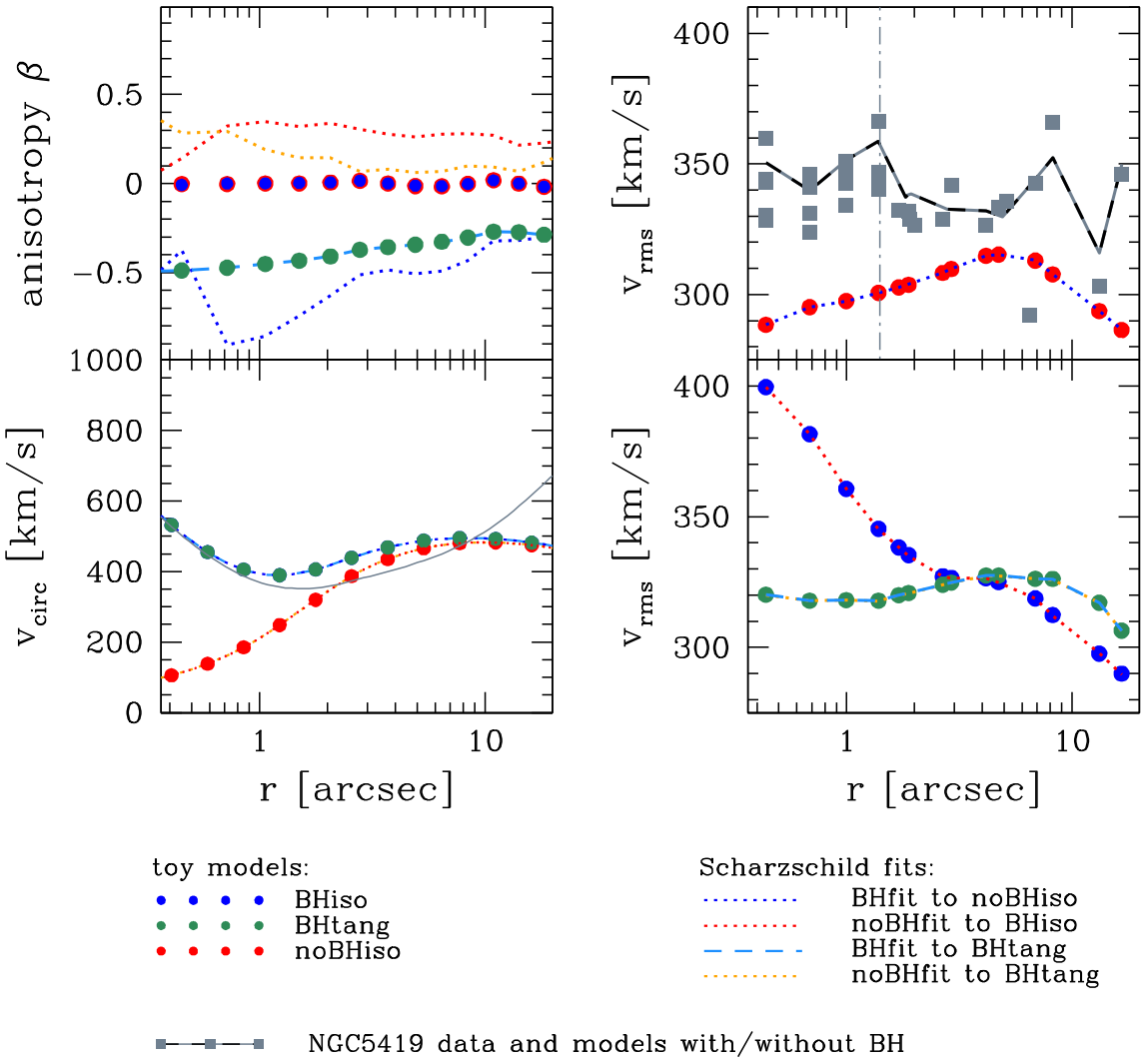

Figure A1. Anisotropy profiles (top-left panel), circular velocity curves (lower-left panel) and projected second-order moments $v_{\rm rms}$ (right-hand panels). Dots show the values from the toy models, while dotted and dashed lines show the fits to the model data. Also shown are the data (grey squares) and best-fitting Schwarzschild model with and without a BH obtained for NGC 5419 (solid grey and dashed black lines). The vertical dot–dashed line indicates the $r_{\rm SOI}$ estimated for NGC 5419's BH (see Section 5). BHiso, noBHiso, and BHtang indicate the isotropic toy models with and without BH and the toy model with BH and tangential anisotropy, respectively. noBHfit and BHfit indicate the fits done assuming no BH and a $M_{\rm BH} = 7 \times 10^9\,{\rm M}_\odot$, respectively. For the toy models and NGC 5419, fits with or without a BH do not produce noticeable differences in the second-order projected velocity moment.

These three (non-rotating) toy models are constructed via orbit superposition. In contrast to the usual application, where the orbital weights are calculated so as to fit the (measured) projected kinematics as well as possible, here we constrain the intrinsic velocity moments of the orbit superposition, and use the library to calculate the corresponding LOSVDs. For the toy models, we assume a spherically symmetric stellar distribution (using the spherically averaged luminosity density of NGC 5419) with a BH in its centre and the framework of Richardson & Fairbairn (2013). For a given stellar mass, BH mass and anisotropy profiles $\beta(r)$ and $\beta'(r)$ in the second- and fourth-order moments, respectively, we solve the Jeans equations up to fourth order. We calculate an orbit library similar to the ones used to fit NGC 5419 but here we calculate the orbital weights such that the respective velocity moments of the orbit superposition reproduce the solutions of the Jeans equations. We then calculate the LOSVDs of the toy model using the same spatial bins on the sky as for NGC 5419. We have tested the method with the analytic (isotropic) models of Baes, Dejonghe & Buyle (2005). For an isotropic Hernquist sphere with various BH masses (as studied in Baes et al. 2005) we find only slight differences, and only in the higher order moments ($\delta H_4 < 0.02$). We have constructed three different toy models, each of which assumes a stellar $\Upsilon = 10$: (1) an isotropic model without a BH ($\beta = \beta' \equiv 0$); (2) an isotropic model with a BH of mass $M_{\rm BH} = 7 \times 10^9\,{\rm M}_\odot$; (3) a model with the same BH mass but with a tangentially anisotropic orbit distribution ($\beta = \beta' < 0$). The tangential anisotropy was chosen such that the model has a roughly constant central $v_{\rm rms}$.

The projected $v_{\rm rms}$ in the isotropic model with (without) a BH increases (decreases), as expected (Fig. A1). Although this has sometimes been taken to be the 'self-evident' behaviour of a system with (without) a BH, it reflects the assumed distribution of orbits in phase space as much as it reflects the underlying mass distribution. To illustrate this, we have fitted the toy models assuming: (1) a $M_{\rm BH} = 7 \times 10^9\,{\rm M}_\odot$ for the case of the toy model without a BH; (2) no BH in the case of the isotropic toy model with a BH, and (3) both no BH and a $M_{\rm BH} = 7 \times 10^9\,{\rm M}_\odot$ in the case of the toy

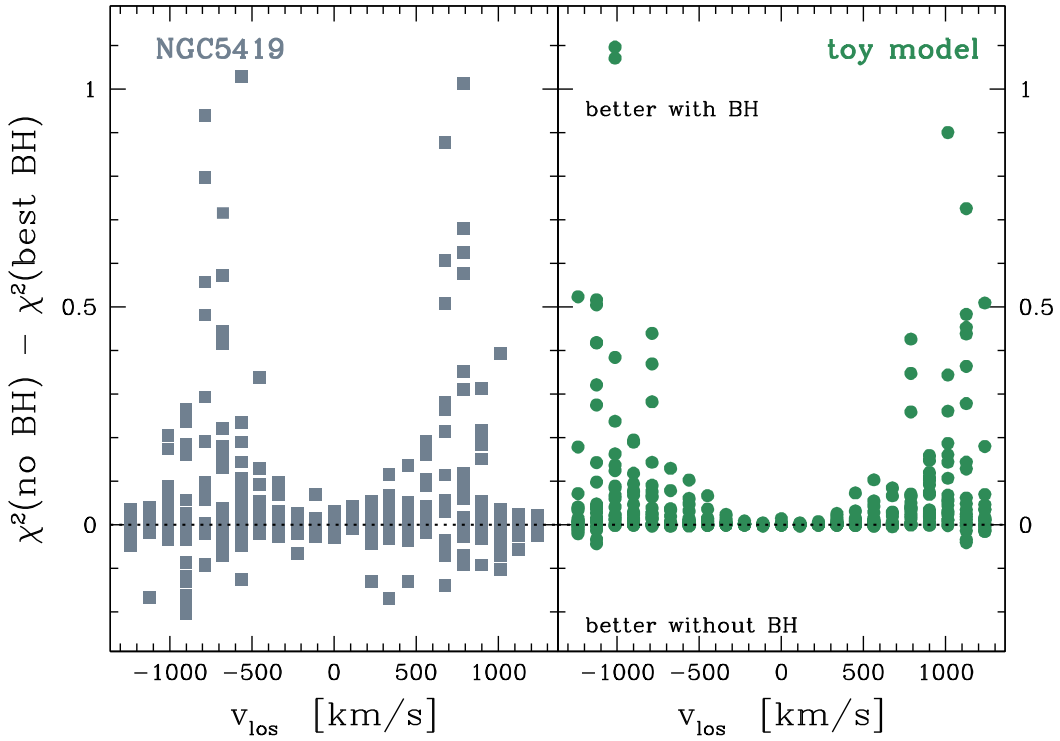

Figure A2. Differences between best-fitting models with and without a BH for NGC 5419 (left) and the toy model with a constant central velocity dispersion (right). Each dot shows the χ^2 difference in a single line-of-sight velocity bin, and the differences are shown over all LOSVDs within the sphere-of-influence radius of the best-fitting BH. The χ^2 is normalized to the same rms as in NGC 5419.

model with flat v_{rms}. Each fit reproduces the second moments of the input LOSVDs perfectly (Fig. A1). A dispersion profile that rises towards the centre can reflect either an isotropic system with a concentrated mass distribution, or a radially anisotropic system without a BH (see Fig. A1 and e.g. BM82, Binney & Tremaine 2008). Conversely, a decreasing velocity dispersion can be due to the lack of a central BH in an isotropic system (with shallow inner mass distribution), or it can indicate tangential anisotropy in such a system with BH. These results are expected to depend on the spatial coverage and resolution of the kinematic data, and on the luminosity constraints for the model.

The second moments provide only limited information about the actual LOSVDs. For the toy model with nearly constant central dispersion, we compare how well the fits with and without a BH reproduce the input LOSVDs in Fig. A2. Despite the fact that the fit without a BH *does* reproduce the second moments of the LOSVDs, it clearly does *not* reproduce the LOSVDs as a whole. The residuals mainly occur at large projected velocities, in the wings of the LOSVDs, and resemble the differences between our best-fitting models with and without a BH for NGC 5419 (Fig. A2).

The Schwarzschild models are fitted to the entire LOSVDs, rather than to a set of velocity moments. In our fits (for both the toy models as well as for NGC 5419), we therefore minimize the difference between the observed and modelled LOSVDs. The Schwarzschild models do not obey any restrictions in the velocity moments, but have the freedom to explore the full range of anisotropies in the moments of any order and in the mixed terms of the velocity moment tensors that are allowed by the tracer density distribution and gravitational potential. This represents the most conservative approach to extract information about the mass structure of an observed galaxy, as the models have the full freedom to utilize all velocity moments to minimize the difference between model and data. Residuals in the fits, as found here between the models with and without a BH for NGC 5419, provide significant evidence for the BH in the galaxy.

This paper has been typeset from a TEX/LATEX file prepared by the author.